Measurements of the velocity distribution for granular flow in a Couette cell

H.T. Fabich[1,2], T.I. Brox[3], D. Clarke[4], J.D. Seymour[5], S.L. Codd[6], P. Galvosas[3], J. Brown[5], A.J. Sederman[1], D.J. Holland[4*]

[1]Department of Chemical Engineering and Biotechnology, University of Cambridge, Philippa Fawcett Drive, Cambridge CB3 0AS, United Kingdom

[2]Now at ABQMR, Inc., 2301 Yale Blvd. SE, Suite C-2, Albuquerque, New Mexico, 87106, USA

[3]School of Chemical and Physical Sciences, Victoria University of Wellington, MacDiarmid Institute for Advanced Materials and Nanotechnology, Wellington, New Zealand

[4]Department of Chemical and Process Engineering, University of Canterbury, Private Bag 4800, Christchurch, New Zealand

[5]Department of Chemical and Biological Engineering, Montana State University, 306 Cobleigh Hall, Bozeman, MT 59717, USA

[6]Mechanical and Industrial Engineering Department, Montana State University, 220 Roberts Hall, Bozeman, MT 59717, USA

Receipt Date: March 13, 2018

*Corresponding Author:
Daniel Holland
daniel.holland@canterbury.ac.nz
Phone: +64 3 369 3785

ABSTRACT

In this study, magnetic resonance velocimetry is used to measure the spatially resolved velocity and velocity fluctuations for granular flow in a Couette cell for four different particle sizes. The largest particles studied (d_p = 1.7 mm) showed significant slip at the inner wall. The remaining particles showed no slip and all exhibit the same behavior in the profiles of the mean velocity and variance of velocity. The measurements demonstrate that the velocity and variance in velocity scale with the inner wall velocity U; the variance does not scale with U^2. The experimental data were compared with a kinetic theory based model of granular flow and a hydrodynamic model. It was found that the shear rate scales with an exponent of 1.5-2.0 with respect to the velocity fluctuations $\sqrt{\langle u_y^2 \rangle}$, compared with the value of 1.0 expected from kinetic theory. The difference in the exponent is consistent with the effect of collective dynamics as described by the hydrodynamic model.

I. INTRODUCTION

Granular flows exist widely in nature, ranging from avalanches to pyroclastic flow, and are also common in industrial processes from pharmaceuticals to oil and gas production. There are many theoretical models of the behaviour of granular materials, but a complete description remains out of reach. One of the challenges of granular flows is that they exhibit phenomena akin to those of solids, liquids and gases, depending on the local conditions [1]. Continuum descriptions of granular flows in the gaseous regime can be derived from the kinetic theory of granular flow, while the solid regime is well modelled using soil mechanics. In general it is the coexistence or transition between granular flow regimes, where continuum granular models tend to break down [2,3]. These transitions are governed by the local velocity or shear rate, the packing density of the particles and perhaps the fluctuations in the particles' velocities about the local mean velocity [4]. Further development of a continuum description of granular flow requires detailed experimental measurements of the motion of particles in well-defined systems. Due to the difficulty of studying granular systems there is relatively little experimental data on the internal dynamics available; most insight has been obtained from numerical simulations in which the motion of each individual particle is tracked [2,5,6]. In this paper, we present magnetic resonance (MR) measurements of the mean velocity and variance in the velocity about the mean in a three-dimensional Couette geometry with a rotating inner wall.

Modelling the granular flow in a Couette geometry is challenging as it is a dense granular flow, with a "granular liquid" flow regime near the rotating wall, and a "granular solid" regime near the stationary wall [3]. There has been some success in developing continuum models for dense granular flows using a simple visco-plastic approach [7]. For inclined plane flows, the visco-plastic model predicts a constant volume fraction of particles with height and a Bagnold scaling for the

velocity , as seen experimentally [3]. In a Couette geometry, the visco-plastic model predicts the formation of shear bands approximately at the transition between the granular liquid and granular solid [8]. However, experimental observations indicate that the size of the shear bands are largely independent of the shear velocity while visco-plastic rheology models suggest a dependence on shear velocity [9].

It has been proposed that a non-local description of granular flow is required to overcome the limitations of the visco-plastic model [2]. Such a non-local rheology model may require an understanding of the fluctuations in the velocity about the local mean and the spatial distribution of the velocities [4]. For example, the spatially dependent variance of these velocity fluctuations $\langle u_k^2 \rangle$ provides information about the energy transport and dissipation across the sample, and is the basis of the concept of granular temperature [10]. Fluctuations that are generated at moving walls are transported through and dissipated in the body of the granular material. The distribution of the magnitude of the fluctuations and the rate of decay across the gap may be related to the transition from a granular gas (higher energy) through to a granular solid [11–13]. However, a consensus has not yet been established for how such effects should be incorporated into a continuum model [2,3].

A variety of techniques exist to characterize the velocity fluctuations [14–19]. However, to date, measurements in a Couette cell have typically been restricted to optical images of the top or bottom surface [17,18], or to observations of only a few particles at very low shear [19]. Observations of the top surface have been justified as being representative of the bulk on the basis that the velocity profile is independent of the height of the bed, as shown using MR experiments [18]. However, measurements at the top surface have indicated that the variance in the velocity fluctuations decay

exponentially [17] while measurements at the bottom surface indicated non-exponential decay [20]. The experimental set up in these experiments differ significantly, but these differences may indicate that the flow on the top and bottom surfaces are not equivalent to that in the bulk.

Magnetic resonance imaging (MRI) can be used to observe the particle dynamics in three-dimensional granular flows. MRI has been used to characterize the velocity in Couette cells and rotating horizontal drums. Initially, such measurements used a spin-tagging approach where an image will show distortion wherever there is motion in the sample [18,21,22]. This approach is limited to observations of the average velocity of particles and extraction of quantitative data is challenging. Pulsed gradient spin echo (PGSE) measurements provide a means of measuring the velocity and velocity distribution in a readily quantitative manner [23]. PGSE measurements are designed such that the phase of the MR signal obtained from each particle is proportional to the strength of an applied gradient and to the displacement of the particle over a fixed time. The mean phase of all particles in a given region is measured and hence the mean velocity of the particles is obtained [24]. PGSE measurements have been used to study the mean flow velocity in both Couette and rotating drum geometries [25–29]. Though not as common as measurements of the mean velocity, it is also possible to determine the distribution of the velocities, and hence the fluctuations, if the experiment is repeated with different gradient strengths. Such measurements have been reported for liquids in many systems [24,30]. For granular materials, these measurements have been reported in rotating drum geometries and fluidized beds [23,27,31], but not in a Couette cell.

In this study, MR will be used to measure the velocity and variance around the mean velocity for dense granular flow in a Couette cell geometry. Measurements are performed in the center of the

geometry, as opposed to on the top or bottom surface. The top surface of the particles is free to expand as the system is sheared allowing significant dilation of the particles near the moving wall. Measurements are performed with four particle types ranging from 0.44 mm to 1.7 mm in diameter.

II. MR THEORY

In studying granular flow, it is important to measure both the mean velocity and the distribution of velocities about the mean. The velocity of an individual particle, $\mathbf{v}_p$, is characterised using Reynolds decomposition as:

$$\mathbf{v}_p = \mathbf{v} + \mathbf{u}, \tag{1}$$

where **v** is the local mean velocity in the sample and **u** is the difference from the local mean velocity, or fluctuation velocity, for particle *p*. The MR signal measured in a PGSE experiment is sensitive to both the mean velocity in a sample and the corresponding distribution around the mean velocity. There are many texts that detail the theory behind MR measurements of motion in a sample [23,24,30,32], however, few studies consider the fluctuations in velocity in granular systems and so the measurement of these by MR will be summarised here.

In an MR experiment, if we consider the time dependent position of a spin to be given by the series $\mathbf{r}(t) = \mathbf{r}_0 + \mathbf{v}_p t + \mathbf{a}_p t^2 + \cdots$, the phase of the MR signal, ϕ, for a single spin following a PGSE experiment is given by:

$$\phi(t) = \gamma \int \mathbf{g}(t') \cdot \left(\mathbf{r}_0 + \mathbf{v}_p t' + \mathbf{a}_p t'^2 + \cdots\right) dt'. \tag{2}$$

where γ is the gyromagnetic ratio, $\mathbf{g}(t')$ is the applied magnetic field gradient, $\mathbf{r}_0$ is initial position, $\mathbf{v}_p$ is particle velocity and $\mathbf{a}_p$ is particle acceleration. For a PGSE experiment, $\int \mathbf{g} dt = 0$ which means the $\mathbf{r}_0$ term becomes zero. We assume the contribution of acceleration is negligible, therefore, if we define a vector, $\mathbf{p} = \gamma \int t' \mathbf{g}(t')\, dt'$, the MR signal may be written:

$$S(\mathbf{p}) = \int \rho(\mathbf{r}) exp(i\mathbf{p} \cdot \mathbf{v} + i\mathbf{p} \cdot \mathbf{u})\, dV, \qquad (3)$$

where $\rho(\mathbf{r})$ is the spin density, or number of protons, at a given position **r** and we have neglected acceleration and higher order terms. If the distribution of the velocity fluctuations in the volume is defined to be given by the probability distribution, η, then the variable of integration can be changed from the volume to the range of velocities. The velocity measurement is only sensitive to motion in the direction of the applied gradient, *k*, hence $\eta = \eta(u_k)$. Assuming that the fluctuation velocity distribution is Gaussian with mean zero and variance $\langle u_k^2 \rangle$, integrating the signal over u_k and normalising by the signal with $p_k = 0$, $S(0)$ gives:

$$\frac{S}{S(0)} = exp(ip_k v_k) exp\left(\frac{-1}{2} p_k^2 \langle u_k^2 \rangle\right). \qquad (4)$$

Thus, the phase of the signal acquired from a PGSE pulse sequence describes the mean velocity in the sample and the magnitude is related to the variance around the mean velocity. Therefore, if a series of experiments are acquired for which the duration of the magnetic field gradient pulses δ, and separation Δ, are kept constant, while the gradient magnitude in direction *k* given by g_k is incremented for both pulses together, the mean velocity can be determined from a fit of a linear equation to the phase, and the variance in velocity from a fit of a parabola to the natural logarithm of the magnitude of the signal. It is worth noting that Eq. 4 holds for small p_k; for large p_k the acceleration and higher order terms become significant and a deviation from parabolic behaviour is observed.

The MR measurement is time-averaged, thus fluctuations in the velocity can arise from variations in the velocity of individual particles about the mean, or from variations of the mean velocity itself over time. In this system, under steady shear, the mean velocity was approximately constant and hence the spatial variance of the velocity fluctuations are estimated by quantifying the signal magnitude at different gradient strengths. In practice, we localize the signal to small volume elements (voxels) within the sample by combining a PGSE experiment with a conventional slice selective, 1D MRI experiment.

III. MATERIALS AND METHODS

Three different types of plant seeds, *lobelia*, *petunia*, and *mustard*, and one size of spherical oil-filled plastic beads were used as solid particles for the granular flow. Plant seeds were used for the solid phase as MRI signal may be acquired from the oil contained within the seeds, similar to the oil-filled particles [21]. The particles were selected for their range in sizes and relatively high sphericity. The diameter and aspect ratio of the *lobelia* seeds was measured using a Morphologi G3 particle characterization system (Malvern Instruments Ltd.). *Lobelia* seeds are visibly oblong in shape. The measured diameter was 0.44 ± 0.03 mm in diameter, averaged along both axes, and the projected aspect ratio was 0.7. The *petunia* seeds were measured using an optical microscope and are approximately spherical with a projected aspect ratio of 0.9 and a diameter of 0.63 ± 0.06 mm. The *mustard* seeds have very high sphericity with no consistent visual variation from this shape; the diameter of the mustard seeds was measured using callipers to be 1.7 ± 0.4 mm. The NMR relaxation times for all varieties of seeds are approximately T_1 = 500 ms, and T_2 = 25 ms. The oil-filled particles are 1 mm in diameter and the size distribution was well below the threshold of the

measurement, ± 0.1 mm. The oil-filled particles are very uniform and have a sphericity of approximately 1. The relaxation times for the oil-filled particles are T_1 = 500 ms, and T_2 = 40 ms.

A. Experimental Setup

Experiments in this work were performed using a Bruker super-wide bore superconducting magnet with a ^{1}H resonance frequency of 300 MHz networked to an AVANCE III spectrometer. The super-wide bore imaging probe was used with a maximum gradient strength of 3.7 G mm^{-1}. A 60 mm birdcage r.f. coil was used for excitation and detection of the signal.

A concentric cylinder rheo-NMR device was used to provide shear across the sample by rotating the inner cylinder. The inner diameter of the larger outer cylinder was 47.3 mm for all experiments. The outer diameter of the smaller inner cylinder varied depending on the particle size. The diameter of the inner cylinder was 32 mm for the *lobelia* and *petunia* seeds, 30.2 mm for the oil-filled particles, and 22.2 mm for the *mustard* seeds giving gap widths of 7.65 mm, 8.55 mm, and 12.55 mm respectively. The gap size increased as the particle size increased to allow for more particles across the gap reducing the potential for jamming. For each sample, a layer of seeds was secured to both the inner and outer walls of the concentric cylinders using double-sided tape to avoid total slip or solid body rotation. Thus, the gap size was 15 d_p (d_p being the seed diameter) for the *lobelia* seeds, 11 d_p for *petunia* seeds, 6.5 d_p for oil-filled particles and 5.4 d_p for *mustard* seeds.

It is noted that the velocity at the inner wall $U = r_i\omega$ where r_i is the inner radius and ω is the angular velocity of the inner cylinder. Each sample was run for U = 17 mm s^{-1} and U = 41 mm s^{-1}. The oil-filled particles were also run at a third shear to give U = 10 mm s^{-1}. In addition, experiments on each sample were run while the sample was stationary.

B. Methods

The gap between the concentric cylinders of the rheo-NMR device, depicted in Fig. 1(a), was filled with sample. The Couette cell was 105 mm deep with a fill depth of 95 mm. The center of the cell was approximately aligned with the center of the magnet, such that measurements were performed at a depth of approximately 45 mm. A PGSE pulse sequence was used with double slice selection as shown in Fig. 1(b). The first part of the pulse sequence, shown in black, is the PGSE portion of the sequence for motion encoding of the spins. The two motion-encoding gradients, applied in *y*, are each on for time, δ. Each gradient pulse is trapezoidal with a ramp time of 150 μs. The displacement observation time, Δ, defines the time from the start of one flow encoding gradient pulse to the start of the next. The motion encoding during the observation time is applied to the whole sample. A 10 mm axial slice was selected between the two orange planes in Fig. 1(a) around the central region of the Couette cell. The second narrow slice of 1 mm thickness is selected in *y*, as shown by the blue planes in Fig. 1(a). The narrow slice in the direction of motion encoding ensures that the curvature of the sample does not have a significant effect on the motion measured providing a mapping $v_y = v_\theta$ of the Cartesian to cylindrical velocity components [33]. Signal is detected from the ensemble average of all spins in the excited slice outlined by the black dashed line in Fig. 1(a). The image is averaged over the slice in *z* and *y* and is acquired along the *x*-dimension, as shown by the red arrow in Fig. 1(a). This provides a spatial velocity profile of $v_y(x) = v_\theta(r)$. The field of view, defined by the gradient in the *x*-direction, is 65 mm. There were 512 points acquired across the sample leading to a spatial resolution of 127 μm per pixel.

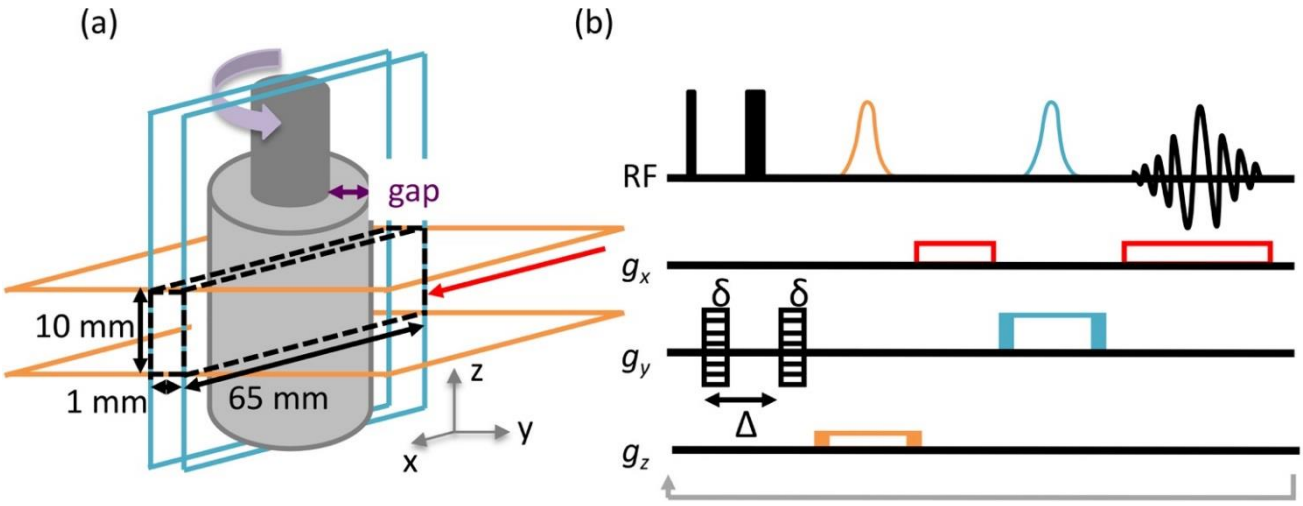

FIG. 1. (a) Schematic diagram of the Couette cell used in this study. The black dashed line indicates the slice over which data is acquired and the red arrow indicates the direction of spatial resolution. (b) The double slice selective PGSE pulse sequence used to image the velocity distribution across the slice. Motion encoding is shown in black at the beginning of the sequence. The two slice selective pulses are colored and matched with the spatially selected slices in (a). The solid portion of the gradients represent the homospoil pulses, extended beyond the soft slice selection. The data is spatially resolved in x, as shown by the red gradient pulses.

Experiments were performed for observation times, Δ, ranging from 1.8 ms to 7 ms, with the flow gradient duration and strength optimised for each observation time. The velocity fluctuations decreased with increasing observation time, but for observation times less than 4 ms the change in mean velocity and velocity fluctuations were small (< 10 %). Hence, an observation time of 3 ms was used for all experiments with δ set to 1 ms. The total echo time for the sequence was about 18 ms. A delay of 2.5 s was allowed for T_1 signal recovery and 32 averages were used with a two-step phase cycle. The flow encoding gradients were ramped from -3.5 G mm^{-1} through zero to 3.4 G mm^{-1} in 64 increments for full sampling of the distribution of velocity. The uncertainty in the measurement of the velocity and velocity fluctuations was calculated from the standard error in the fit of the phase and magnitude of the signal, respectively, at each point.

The signal magnitude across the Couette cell varies, likely due to an interaction of B_1 with the B_0 field creating a heterogeneous effective magnetic field. This variation is present in both flowing and stationary experiments. To correct for this effect, the complex, spatially resolved, frequency domain data for all experiments were divided by a measurement acquired under stationary conditions. There is also an apparent reduction in magnitude near the inner wall, which is dependent on the inner wall velocity. The signal intensity is reduced in part due to the lower density of seeds where motion is highest. However, in these experiments the main causes of the reduced signal intensity are the velocity shear across a pixel, or fluctuations in the velocity of particles about the local average velocity [34]. Each of the gradients in the system can act as motion encoding gradients and hence impart a phase to the signal arising from each particle. If the velocity of the particles in a given position is not constant, then these phases will add incoherently and hence reduce the signal intensity. Here the most significant motion encoding from the imaging gradients arises from the read gradient. The faster the motion of the sample, the faster the signal dephases and the lower the signal magnitude. This additional attenuation of the signal makes quantitative measurement of the solid fraction challenging. Therefore, only measurements of the mean velocity and the variance around the mean velocity are considered in this work.

IV. RESULTS

A. Mean velocity

Velocity profiles are shown in Fig. 2 for inner wall velocities of $U = 17$ mm s^{-1} and for $U = 41$ mm s^{-1}. The signal intensity for $U = 41$ mm s^{-1} is shown as a solid grey line as visual reference of the position of the gap. A reduction in signal magnitude near the moving wall is observed, as mentioned in the previous section. The velocity profiles shown are for the y-component of the velocity, i.e.

perpendicular to the direction of the image and effectively v_θ of the cylinder. As the inner cylinder is rotating, the particles in the left-hand gap appear to be moving away from the observer and those on the right-hand side are moving toward the observer. This leads to a negative velocity profile on the left-hand side of the gap and a positive velocity profile on the right-hand side of the gap. The shape of the profile shows a maximum at the inner wall, where a seed has been secured to prevent slip at the boundary. The velocity quickly decays to approximately zero, well before reaching the outer wall, where again, the seeds have been secured to the wall to prevent solid body rotation of the sample.

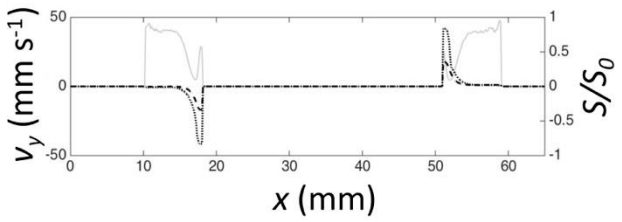

FIG. 2. Velocity and signal magnitude profiles across the gap are shown for two different inner wall velocities, U = 17 mm s^{-1} (dashed) and U = 41 mm s^{-1} (dotted). The normalized 1D signal intensity profile for U = 41 mm s^{-1} is shown in grey. For both shear rates the velocity profile decays to approximately zero well before the stationary, outer wall.

Figure 3 shows the velocity profiles for all four types of particles used in this study for inner wall velocities of 17 mm s^{-1} and 41 mm s^{-1}. The velocity profiles were normalized by dividing obtained velocities by the inner wall velocity. Error bars give the 95% confidence interval for the fit to the phase of the signal. Figure 3(a) shows velocity profiles for *lobelia* seeds in blue, Fig. 3(b) for *petunia* seeds in purple, Fig. 3(c) for oil-filled particles in black, and Fig. 3(d) for *mustard* seeds in yellow. This color scheme will be used through the remainder of the results to differentiate the different particles. In Fig. 3 an inner wall velocity of 17 mm s^{-1} is indicated by (+), 41 mm s^{-1} by (o) and, for the oil-filled particles, 10 mm s^{-1} by (■). For the three smaller particles used, Fig. 3(a-c), the

velocity profiles all show a smooth decrease in the velocity of the particles from the inner wall. The velocities measured scale with the inner wall velocities. The shape of the velocity profiles for both shear rates is indistinguishable, confirming previous results for the top and bottom surface of a Couette that the shape of the velocity profile across the gap does not depend on the shear rate [17,18,35]. However, the normalized profiles for *mustard* seeds are not consistent with the profiles for the other particles. The velocity profile shows a step change between the particle stuck to the wall and the next particle, one away from the wall. This step change is indicative of slip between the particles attached to the wall and the first free particle. The *mustard* seeds were used with the largest available gap, but there were still only 5.4 particles across the gap. Either the large gap size or the small number of particles was such that slip dominated at the inner wall. Interestingly, the velocity of the particles immediately next to the inner wall was still approximately proportional to the inner wall velocity, even in the presence of significant slip. However, from this point forward, only data for the three smaller particles, the *lobelia*, *petunia*, and oil-filled particles, will be analyzed to avoid complications arising from slip.

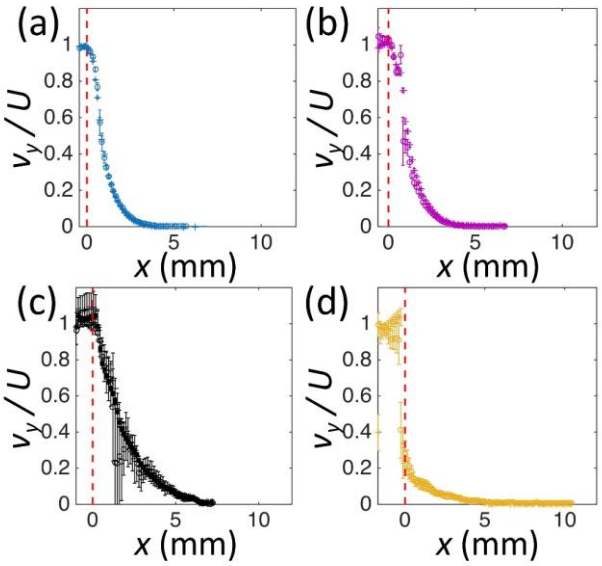

FIG. 3. Normalized velocity profiles for each type of particle (a) *lobelia* seeds, (b) *petunia* seeds, (c) oil-filled particles, (d) *mustard* seeds at different inner wall velocities of 17 mm/s (+) and 41 mm/s (o). A third velocity of 10 mm/s (■) is shown in (c) for the oil-filled particles. The *x*-position of the first free moving particle is set to zero hence the red line shows the outer edge of the particle attached to the wall. The velocity profiles are independent of shear for all particles. The *mustard* particles are much larger than the other three particles and show slip between the particle attached to the wall and the first free particle.

Figure 4 show the normalized velocity profiles rescaled against dimensionless distance x/d_p, where d_p is the average particle diameter. The velocity profiles collapse onto the same curve close to the inner wall. In this region, the scaled velocities follow an exponential decay with dimensionless distance. The characteristic length scale associated with the decay in velocity is 1.3-2 d_p. Previous research in Couette cells has found the decay constant for the velocity to be between 2 and 5 [17,20]. Previous measurements in the Couette geometry show exponentially decreasing velocity initially with the rate approaching a Gaussian decay further from the rotating wall for both spherical and non-spherical particles [36]. Exponential behaviour is generally associated with correlated dynamics, while Gaussian behavior is associated with non-correlated dynamics [37]. In the context of granular flow, correlated dynamics may arise when the particles are driven with a fixed velocity and the solid fraction is such that there are relatively few collisions between particles. On the other hand, non-

correlated dynamics may be associated with particles vibrating within a relatively fixed set of neighbours, analogous to caging in glassy materials. The results presented here suggest that near the moving wall, particles may exhibit correlated dynamics. Away from the moving wall, approximately 5 d_p for oil-filled and *petunia*, and 8 d_p for *lobelia*, the rate of decay increases. We hypothesise that the ellipsoidal shape of the lobelia seeds causes increased correlation and delays the transition to a non-exponential decay. Such a delay could arise from the rotational dynamics of the particles causing a decrease in packing efficiency, analogous to the Jeffrey orbits for rotation of ellipsoidal particles under shear [38].

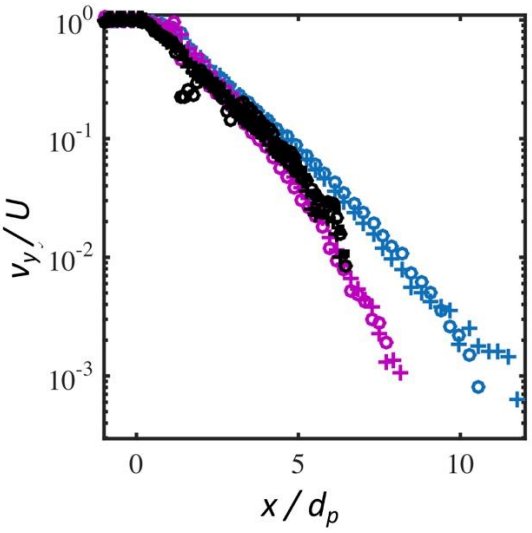

FIG. 4. Velocity profiles are plotted against the number of particles across the gap. *Lobelia* are shown in blue, *petunia* in purple, and oil-filled in black. *Lobelia* and *petunia* seeds are shown for inner wall velocities of 17 mm/s (+) and 41 mm/s (o). Oil-filled particles are shown for 10 mm/s (■) in addition to the other wall velocities. All particles show a similar rate of decay for the first five particles. Further from the wall, the *petunia* and oil-filled particles show a more rapid decay than the *lobelia* seeds.

B. Variance of velocity

Figure 5 illustrates the measurement of the spatial variance of the velocity fluctuations from the signal intensity of the velocity encoded MR measurement. The experimental data is for a sample of *lobelia* seeds at U = 17 mm s^{-1}. Figure 5(a) shows the signal intensity profile across the gap with no

gradient applied, g_y = 0 G mm^{-1} and for a gradient of g_y = -3.5 G mm^{-1}. The left hand side of Fig 5(a) is aligned with the inner rotating wall, while the right hand side is the outer stationary wall. On the left-hand side of the gap, where the particle velocities were greatest, it is easy to distinguish between the two measurements. Toward the right-hand side of the gap, where there is almost no flow, no significant difference can be seen between the signal intensities, indicating the fluctuations decrease toward zero in the region of no flow.

To illustrate the calculation of the variance in the velocity, two points are selected in Fig. 5(a), a green point in the high flow region and a purple point in the low flow region. Experiments are run with 64 gradient strengths incremented from g_y = -3.5 G mm^{-1} to g_y = 3.4 G mm^{-1}. The signal magnitude is normalized to the maximum signal acquired for a flow gradient of g_y = 0 G mm^{-1}. Figure 5(b) shows the log of the normalized signal plotted against p_y where $p_y = \gamma\delta\Delta g_y$ for both the green and purple markers in Fig. 5(a). The green squares on the left-hand side of Fig. 5(a) are in a region with high velocity and high variance in the velocity. This is shown by the green points in Fig. 5(b), which outline a clear parabolic shape. The purple squares, nearer the middle of Fig. 5(a), are in a region with very slow flow. The purple points in Fig. 5(b) show the change in the signal magnitude with increasing gradient magnitude outlining a very shallow parabolic shape indicating almost no variance in the velocity at such low flow. Also note that here we calculate p_y from the PGSE gradient strength only, however, there is also a contribution from the slice gradient which causes the first order offset seen in Fig. 5(b). The two sets of data are fit to a Gaussian, as shown in Fig. 5(b), and the coefficient of p_y^2 is proportional to the variance in the velocity, $\langle u_y^2 \rangle$, as given in Eq. 4. The variance in the velocity is calculated for each point across the gap shown in Fig. 5(a) and these coefficients are plotted in Fig. 5(c) with error bars representing the 95% confidence interval..

The green square represents the green fit from Fig. 5(b) and the purple square represents the purple fit.

It is important to consider the limitations of detection of the measurement. The decay of the signal in static samples gives a lower detection limit of 0.8 $mm^2\ s^{-2}$ for the variance of the velocity. This limit of detection likely arises from acoustic vibration [39]. In addition to the local fluctuations in velocity, shear contributes to the observed variance of velocity due to the spread of velocities across the voxel [40]. If we assume a constant velocity gradient with a difference in velocity Δv across a voxel, this corresponds to a contribution to the variance of $\langle u_y^2 \rangle = \frac{(\Delta v)^2}{12}$. Figure 3 indicates that shear gives a difference in velocity across a pixel of at most 2 $mm\ s^{-1}$, so the contribution to the variance of velocity arising from shear is 0.3 $mm^2\ s^{-2}$. This variance is below the limit of detection, and hence velocity fluctuations dominate in these experiments. The maximum velocity fluctuation that can be measured is limited by attenuation arising from the imaging gradients themselves. Attenuation caused by the imaging gradients does not directly influence the measurement, as we calculate attenuation from changes in signal intensity with respect to changing flow encoding gradient strength. However, if the variance of the particles velocities is too great, the imaging gradients alone will cause the signal to decay close to the noise. For this reason, measurements of the variance of velocity in excess of 200 $mm^2\ s^{-2}$ were unreliable here. At 41 $mm\ s^{-1}$, variances in the velocity of this size occurred for particles within 1 mm of the inner wall for all particles and for most of the gap for the oil-filled particles. For this reason, experiments with the oil-filled particles were repeated for U = 10 $mm\ s^{-1}$, and the U = 41 $mm\ s^{-1}$ results are not shown. Thus, the experiments are able to measure variances in the velocity between about 0.8 $mm^2\ s^{-2}$ and 200 $mm^2\ s^{-2}$.

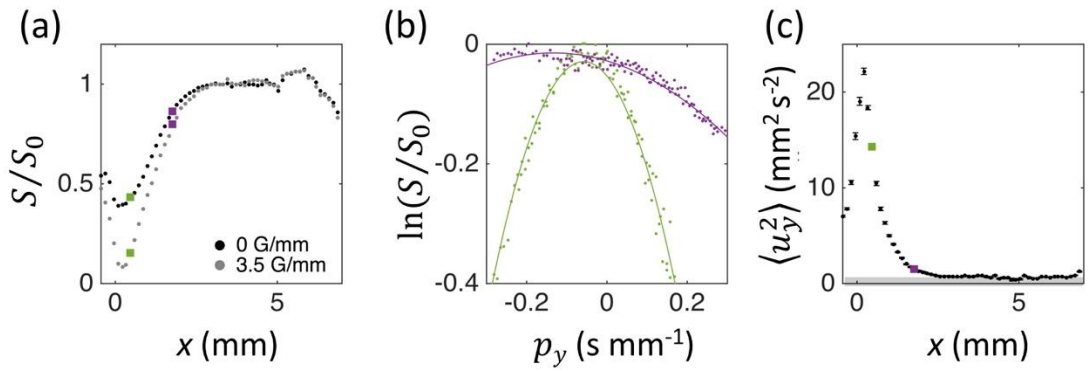

FIG. 5. Illustration of the calculation of the variance in velocity from flow encoded 1D profiles to for *lobelia* seeds with Δ = 3 ms and an inner wall velocity U =17 mm s^{-1}. (a) Profiles across a gap for two different gradient strengths. The green squares mark a high shear region and the purple squares mark a lower shear region. (b) Change in signal intensity with p_y for high flow (green) and low flow (purple) points as were depicted on profiles shown in (a). The squared coefficient of the parabolic fit is used to calculate the variance in the velocity $\langle u_y^2 \rangle$ and is plotted as a function of the position across the gap in (c) with error bars representing the 95% confidence interval of the fit. The green and purple squares indicate the respective fits from (b) and the grey shaded region indicates the region below the lower limit of detection in these measurements.

Figure 6 shows the variance of the velocity fluctuations for each particle type and for U = 10 mm s^{-1}, U = 17 mm s^{-1} and for U = 41 mm s^{-1}. The error bars indicate the 95% confidence interval of the fit shown in Fig. 5(b). The variances in the velocity initially increase in the vicinity of the moving wall, but then decrease with distance from the moving wall. The decay is non-linear and appears to follow an approximately exponential trend. The variance in the velocity increases with increasing inner wall velocity and increases slightly with increasing particle size.

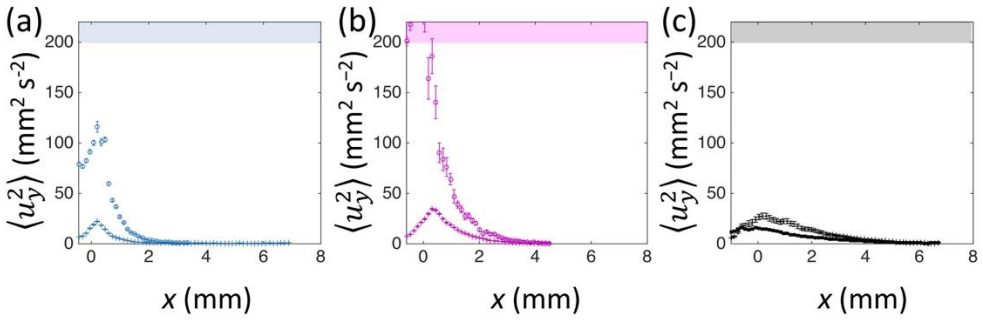

FIG. 6. The variance in the velocity is shown for (a) *lobelia*, (b) *petunia*, and (c) oil-filled particles for U = 10.0 mm s^{-1} (■), U = 17 mm s^{-1} (+), U = 41 mm s^{-1} (o). The shaded regions indicate the region above the limits of the measurement technique.

Figure 7 shows the variance as a function of the dimensionless distance across the gap. The variance here was normalized by $U(gd_p)^{0.5}$, where g is gravitational acceleration [36]. Using this comparison, the curves for the *lobelia* seeds, *petunia* seeds and oil-filled particles all collapse onto almost the same line, independent of the shear rate and particle size or type. Thus, the variance of the fluctuations scales with the wall velocity, U, and not U^2. The decay for the *petunia* and *lobelia* seeds can be measured over more particles due to their smaller diameter. The measurements show that the variances in the velocity remain approximately exponential across the gap from 1 to 6 d_p, indicating that the fluctuations transmit themselves in a correlated fashion over the measurable range. The characteristic length scale associated with this exponential decay is approximately 1 – 1.5 d_p, slightly less than the decay length for the velocity and significantly less than the decay length seen in previous experiments using glass beads [17]. The deviation from an exponential decay observed in the velocity profiles in Fig. 4 is not seen in these measurements of the variance. This is likely due to the measurements of the variance being below the threshold of the measurement at distances in excess of ~6 d_p, which corresponds to the point at which the decay in the velocity profile, shown in Fig. 4, deviates from an exponential decay. Interestingly, at distances in excess of ~4 d_p, the decay of fluctuations for the *lobelia* seeds slows from the initial exponential rate. It is unclear at this stage

whether this change is related to the persistence of the exponential decay in the mean velocity seen in Fig. 4 for these particles.

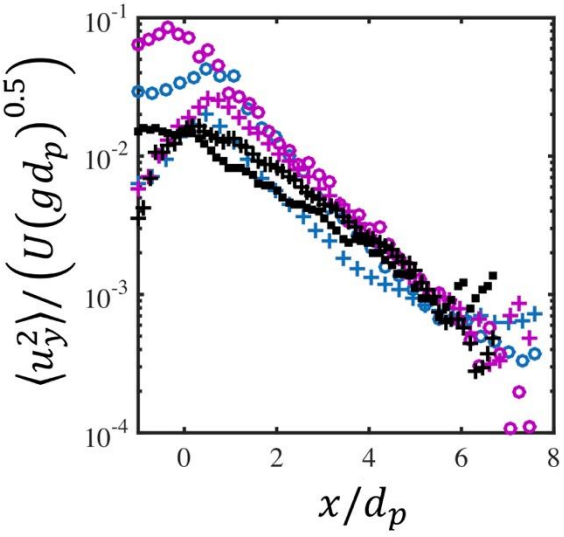

FIG. 7. The normalized variance in velocity is shown for *lobelia* (blue), *petunia* (purple), and oil-filled particles (black) for U = 10.0 mm s^{-1} (■), U = 17 mm s^{-1} (+), and U = 41 mm s^{-1} (o). The decay of the variance plotted against the number of particles across the gap is independent of inner wall velocity and particle size.

V. DISCUSSION

There has been extensive work on the rheology of granular flows, and the related area of soft condensed matter, much of which has recently been reviewed [41]. It is interesting to consider our measurements in light of this work and hence explore the apparent rheology suggested. Here we consider the region in which an exponential decrease in velocity and variance in velocity with gap position were observed. It is expected that the rheology will depend on the shear rate, local solid packing, confining pressure and the variance in the velocity of the particles. From our experiments, the local shear rate $\dot{\gamma}$ is obtained from the gradient of the velocity profile:

$$\dot{\gamma} = \frac{dv_\theta(r)}{dr}, \tag{5}$$

where v_θ is the local mean velocity of the particles in the azimuthal direction. Here we use a 4th-order noise-robust method to calculate the shear rate from the velocity measurements [42]. In a Couette geometry at steady state and with no variation in velocity around the annulus or with height, a momentum balance in cylindrical coordinates shows that $r^2\tau$ is constant everywhere, τ being the shear stress at a given r. Hence a local shear stress τ at any position *r* can be calculated from the inner wall shear stress τ_{iw} according to:

$$\tau = \frac{r_{iw}^2 \tau_{iw}}{r^2}, \tag{6}$$

where r_{iw} is the position of the inner wall. Although it was not possible to measure the torque, and hence shear stress at the wall, with the present set up, Eq. 6 is used to determine the shear stress to within a constant anywhere across the gap. The experiments performed here could not yield the solid fraction. Thus, we consider two simple rheological models of granular flow in the context of the shear stress, shear rate and velocity fluctuations.

Firstly, we consider the typical granular rheology model which takes the form:

$$\tau = \mu P, \tag{7}$$

where μ relates the shear and normal stresses and *P* is the normal stress (pressure). This formulation is potentially consistent with both dense phase kinetic theory [41] and non-local rheology [44] models. It is expected that μ will be a function of the solid fraction, confining pressure, shear rate and variance in velocity. For example, for simple shear flow, the kinetic theory of granular flow yields [5,43]:

$$\mu = \frac{\tau}{P} = \frac{d_p \dot{\gamma} F(\phi, e)}{\sqrt{\langle u_y^2 \rangle}}, \tag{8}$$

where $F(\phi, e)$ is some function of the solid fraction ϕ and the coefficient of restitution *e*. Noting that the pressure is approximately constant across the cross-section, and ignoring variation in solid fraction, Eqns. 6 and 8 are combined to yield:

$$\dot{\gamma} r^2 \propto \sqrt{\langle u_y^2 \rangle}. \tag{9}$$

Thus, following kinetic theory, we expect the shear rate to scale with the square root of the velocity fluctuations.

Alternatively, the problem may be approached using a hydrodynamic model, as in [17]:

$$\tau = \eta \dot{\gamma}, \tag{10}$$

where η is an apparent viscosity that will be a function primarily of the solids packing and velocity fluctuations. It is expected that the viscosity will diverge as it approaches the close packing limit in the dense regions of the bed. Following [17], the viscosity is assumed to diverge as it approaches the close packing limit with a power β, where $\beta = 1$ under the Enskog model but is expected to be greater than 1 if collective dynamics are important. Under these conditions, the shear rate is expected to scale with the velocity fluctuations according to:

$$\dot{\gamma} \propto \sqrt{\langle u_y^2 \rangle}^{(2\beta - 1)}. \tag{11}$$

Previous research has found $\beta \cong 1.5$ for photoelastic disks and 1.8 for glass beads, consistent with the presence of collective dynamics in dense granular flows [17]. These values imply an exponent greater than unity, whereas the model given by Eq. 9 implies a value of unity.

Here, each of these models is considered by plotting the relationship between shear rate and velocity fluctuations in Fig. 8 (i.e. Eq. 11) along with the plot for Eq. 9 (inset). Here only the component of the velocity in the *y*-direction was measured, hence the comparison with the theoretical models implicitly assumes isotropy of the fluctuations. These figures show that for the faster moving particles the apparent viscosity follows a power law model with respect to the variance in the velocity for all three particle types. At lower velocities and smaller variance in the velocity, the data show a distinct curvature on the log scale. This curvature is likely due to the density approaching the close packing limit, causing a strong divergence of the viscosity. Further experiments are required in which quantitative measurements of ϕ are possible to clarify this effect.

The exponential decay regions of the plots shown in Fig. 8 were fitted with a power law model. The *petunia* and oil-filled particle results indicate the shear rate $\dot{\gamma}$ scales with the square root of the velocity fluctuations $\left(\sqrt{\langle u_y^2 \rangle}\right)$ with an exponent of 2.0 ± 0.1 and the *lobelia* scales with an exponent of 1.5 ± 0.1. The calculated exponent was independent of the shear rate for all three particle types. The scaling is also independent of the form of the equation, i.e. the inset yields a similar slope to the main figure, since in this case the gap is small relative to the radius and the r^2 term is approximately constant. Thus, it is expected that both Eq. 9 and Eq. 11 could be applicable here. The measured exponent is greater than that predicted by Eq. 9 (which predicts an exponent of 1). From Eq. 11, the measured exponent is consistent with a value for $\beta = 1.5 \pm 0.1$ for *petunia* and the oil-filled particles and $\beta = 1.3 \pm 0.1$ for *lobelia*. The results for petunia and oil-filled particles are consistent with the analysis in [17]. The lower β value for the lobelia seeds may be linked to the particle shape, given the different exponents measured for the spherical and non-spherical particles here. However, in any

case, these results indicate that the granular material exhibits cooperative dynamics and a faster divergence than the Enskog model alone predicts on approach to the close packing limit.

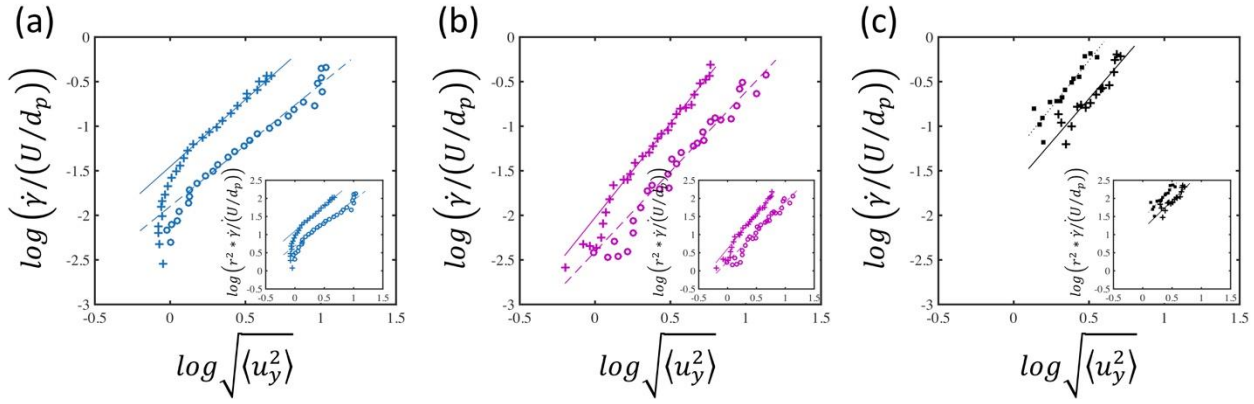

FIG. 8. Plot of inverse shear against the RMS variance in the velocity for (a) *lobelia*, (b) *petunia*, and (c) oil-filled particles. For each particle type two inner wall velocities are analyzed, U = 17 mm s^{-1} (+), U = 41 mm s^{-1} (o) and for oil-filled particles U = 10.0 mm s^{-1} (■). The fit to the data is shown as a solid line for U = 17 mm s^{-1}, dashed line for U = 41 mm s^{-1} and dotted for U = 10 mm s^{-1}. The insets show the same data plotted according to Eq. 9.

VI. CONCLUSIONS

This study has used MRI to acquire velocity profiles and velocity fluctuation profiles across the gap in a Couette cell. To the best of our knowledge this is the first-time data for the variance about the mean velocity have been measured non-invasively in the centre of a 3D Couette cell. The measurements demonstrate that the velocity scales with the inner wall velocity U, while the variance scales approximately with $U\left(gd_p\right)^{0.5}$. Four particle types were measured and the data indicate that the same relationship holds for the three smallest particles, where no slip was observed, whilst the largest particles (*mustard* seeds) exhibited significant slip and hence a different behavior. The results of the experiments are largely consistent with previous experimental observations of the top and bottom surface of a Couette, and with numerical simulations.

The measurements were also used to infer that the apparent rheology of the granular material followed a power law model with respect to the local variance in the velocity of the particles, at least in regions where the particles were moving freely. The power law relationship indicates scaling of the velocity fluctuations with an exponent greater than 1, in contrast to kinetic theory analysis; it is consistent with the hydrodynamic model in which collective dynamics are significant. The analysis of the rheology presented here was restricted to the power law region of the shear rate – velocity variance curve. A deviation from this behaviour was seen close to the stationary wall, perhaps indicative of shear banding or shear localisation [41]. In the future, measurements such as those presented here could be used to investigate the connection between shear banding, yield stress and the velocity fluctuations.

ACKNOWLDEGEMENTS

The authors would like to thank Fred C. Gloeckner & Co., Inc for arranging donations of plant seeds from the Takii Seed Company and the Pan American Seed Company. HTF would like to acknowledge the financial support of the Gates-Cambridge Trust. The NMR experiments were conducted at the MSU MR Lab, JRB, JDS and SLC thank the NSF MRI program and the M.J. Murdock Charitable Trust for equipment funding.

VII. REFERENCES

[1] H. M. Jaeger, S. R. Nagel, and R. P. Behringer, Rev. Mod. Phys. **68**, 1259 (1996).
[2] P. Jop, Comptes Rendus Phys. **16**, 62 (2015).
[3] Y. Forterre and O. Pouliquen, Annu. Rev. Fluid Mech. **40**, 1 (2008).
[4] O. Pouliquen and Y. Forterre, Philos. Trans. R. Soc. London A Math. Phys. Eng. Sci. **367**, 5091 (2009).
[5] S. Chialvo and S. Sundaresan, Phys. Fluids **25**, 070603 (2013).
[6] G. Koval, J.-N. Roux, A. Corfdir, and F. Chevoir, Phys. Rev. E **79**, 021306 (2009).
[7] P. Jop, Y. Forterre, and O. Pouliquen, Nature **441**, 727 (2006).
[8] O. Pouliquen, C. Cassar, P. Jop, Y. Forterre, and M. Nicolas, J. Stat. Mech. Theory Exp. **2006**, P07020 (2006).
[9] Z. Tang, T. A. Brzinski, M. Shearer, and K. E. Daniels, Soft Matter **14**, 3040 (2018).
[10] I. Goldhirsch, Powder Technol. **182**, 130 (2008).
[11] J. T. Jenkins, Phys. Fluids **18**, 103307 (2006).
[12] N. Mitarai and H. Nakanishi, Phys. Rev. E **75**, 031305 (2007).
[13] D. Vescovi, C. di Prisco, and D. Berzi, Int. J. Numer. Anal. Methods Geomech. **37**, 2937 (2013).
[14] N. Menon and D. J. Durian, Science (80-.). **275**, 1920 (1997).
[15] R. Wildman and D. Parker, Phys. Rev. Lett. **88**, 064301 (2002).
[16] D. Candela, C. Huan, K. Facto, R. Wang, R. W. Mair, and R. L. Walsworth, Granul. Matter **9**, 331 (2007).
[17] L. Bocquet, W. Losert, D. Schalk, T. Lubensky, and J. Gollub, Phys. Rev. E **65**, 011307 (2001).
[18] D. M. Mueth, G. F. Debregeas, G. S. Karczmar, P. J. Eng, S. R. Nagel, and H. M. Jaeger, Nature **406**, 385 (2000).
[19] P. Wang, C. Song, C. Briscoe, and H. A. Makse, Phys. Rev. E **77**, 061309 (2008).
[20] D. Mueth, Phys. Rev. E **67**, 011304 (2003).
[21] M. Nakagawa, S. A. Altobelli, A. Caprihan, E. Fukushima, and E. Jeong, Exp. Fluids **16**, 54 (1993).
[22] K. Yamane, M. Nakagawa, S. A. Altobelli, T. Tanaka, and Y. Tsuji, Phys. Fluids **10**, 1419 (1998).
[23] E. Fukushima, Annu. Rev. Fluid Mech. **31**, 95 (1999).
[24] P. T. Callaghan, *Principles of Nuclear Magnetic Resonance Microscopy* (Clarendon Press, Oxford, 1991).
[25] N. Huang, G. Ovarlez, F. Bertrand, S. Rodts, P. Coussot, and D. Bonn, Phys. Rev. Lett. **94**, 028301 (2005).
[26] G. Ovarlez, F. Bertrand, and S. Rodts, J. Rheol. (N. Y. N. Y). **50**, 259 (2006).
[27] J. Seymour, A. Caprihan, S. Altobelli, and E. Fukushima, Phys. Rev. Lett. **84**, 266 (2000).
[28] A. Caprihan and J. D. Seymour, J. Magn. Reson. **144**, 96 (2000).
[29] P. Moucheront, F. Bertrand, G. Koval, L. Tocquer, S. Rodts, J.-N. Roux, A. Corfdir, and F. Chevoir, Magn. Reson. Imaging **28**, 910 (2010).
[30] C. J. Elkins and M. T. Alley, Exp. Fluids **43**, 823 (2007).
[31] D. J. Holland, L. F. Gladden, C. R. Müller, J. S. Dennis, and A. J. Sederman, Powder Technol.

182, 171 (2008).
[32] L. F. Gladden and A. J. Sederman, J. Magn. Reson. **229**, 2 (2013).
[33] S. Kuczera and P. Galvosas, J. Magn. Reson. **259**, 135 (2015).
[34] P. T. Callaghan, *Translational Dynamics & Magnetic Resonance: Principles of Pulse Gradient Spin Echo NMR* (Oxford University Press, New York, 2011).
[35] R. . Behringer, D. Howell, L. Kondic, S. Tennakoon, and C. Veje, Phys. D **133**, 1 (1999).
[36] G. D. R. Midi, Eur. Phys. J. E **14**, 341 (2004).
[37] N. Goldenfeld and L. P. Kadanoff, Science (80-.). **284**, 87 (1999).
[38] G. B. Jeffery, Proc. R. Soc. A Math. Phys. Eng. Sci. **102**, 161 (1922).
[39] N. K. Bar, J. Karger, C. Krause, W. Schmitz, and G. Seiffert, J. Magn. Reson. **113**, 278 (1995).
[40] D. O. Kuethe and R. J. Herfkens, Magn. Reson. Med. **10**, 57 (1989).
[41] D. Bonn, M. M. Denn, L. Berthier, T. Divoux, and S. Manneville, Rev. Mod. Phys. **89**, 1 (2017).
[42] P. Holoborodko, (2008).
[43] V. Garzó and J. W. Dufty, Phys. Rev. E **59**, 5895 (1999).
[44] K. Kamrin and G. Koval, Phys. Rev. Lett. **108**, 1 (2012).